Nanoscale

PAPER

Multi-heteroatom-doping promotes molecular oxygen activation on polymeric carbon nitride for simultaneous generation of H_2O_2 and degradation of oxcarbazepine†

Derui Chen,[a] Bingling Yao,[a] Xinyu Zhi,[a] Chang Tian,[a] Minghao Chen,[a] Siyi Cao,[a] Xinyu Feng,[a] Huinan Che, [ID] *[a] Kan Zhang [ID] *[b] and Yanhui Ao [ID] [a]

Simultaneously realizing the efficient generation of H_2O_2 and degradation of pollutants is of great significance for environmental remediation. However, most polymeric semiconductors only show moderate performance in molecular oxygen (O_2) activation due to the sluggish electron–hole pair dissociation and charge transfer dynamics. Herein, we develop a simple thermal shrinkage strategy to construct multi-heteroatom-doped polymeric carbon nitride (K, P, O-CN$_x$). The resultant K, P, O-CN$_x$ not only improves the separation efficiency of charge carriers, but also improves the adsorption/activation capacity of O_2. K, P, O-CN$_x$ significantly increases the production of H_2O_2 and the degradation activity of oxcarbazepine (OXC) under visible light. K, P, O-CN$_5$ shows a high H_2O_2 production rate (1858 µM h^{-1} g^{-1}) in water under visible light, far surpassing that of pure PCN. The apparent rate constant for OXC degradation by K, P, O-CN$_5$ increases to 0.0491 min^{-1}, which is 8.47 times that of PCN. Density functional theory (DFT) calculations show that the adsorption energy of O_2 near phosphorus atoms in K, P, O-CN$_x$ is the highest. This work provides a new idea for the efficient degradation of pollutants and generation of H_2O_2 at the same time.

1. Introduction

Oxcarbazepine (OXC), as a kind of refractory organic pollutant in wastewater, is strongly toxic and highly persistent, posing a serious threat to the water environment.[1–4] Thus, it has become urgently necessary to find solutions all over the world to reduce the toxicity of refractory organic wastewater throughout the process of degradation.[5] Recently, several studies have concentrated on the use of advanced oxidation technologies (AOPs) to quickly remove organic contaminants from water.[6–8] Nevertheless, to promote the catalytic oxidation process and form reactive oxygen species (ROS), such as hydroxyl radicals (˙OH), superoxide radicals (˙O$_2^-$) and singlet oxygen ($^1O_2$),[9,10] it is often essential to add a strong oxidant (*e.g.*, H_2O_2 or persulfate) or input energy (*e.g.*, light or electricity) in most AOP

techniques.[11,12] Although these methods promote the generation of a large number of ROS and effectively degrade organic pollutants, the price is higher energy use and environmental pollution.[13] Therefore, there is an increasingly urgent need to develop an environmentally friendly strategyy that has simple operation and mild reaction conditions to solve the problem of water pollution.

Molecular oxygen (O_2), as a non-toxic, pollution-free and cheap oxidant, has many advantages over other oxidants, playing an important role in the field of refractory organic wastewater treatment.[14] The activated O_2 can stimulate the production of ROS, including $^1O_2$, ˙OH, ˙O$_2^-$ and hydrogen peroxide (H_2O_2), which are the main active substances in the degradation process of organic pollutants. It is worth noting that polymeric carbon nitride (PCN) has attracted extensive attention from many researchers in O_2 activation ($O_2 \rightarrow$ ˙O$_2^- \rightarrow$ $H_2O_2 \rightarrow$ ˙OH).[15–22] Among them, the *in situ* formation of ˙OH is of great significance for environmental remediation, which is due to its strong oxidation capacity.[23–25] However, a one-step single-electron oxygen reduction reaction (ORR) is easy to achieve, resulting in ˙O$_2^-$ radicals as the main ROS. Considering that the photocatalytic properties of these charge transfer processes are related to the lifetime and concentration of the carriers that can reach the catalyst surface, great efforts

[a]Key Laboratory of Integrated Regulation and Resource Development on Shallow Lakes, Ministry of Education, College of Environment, Hohai University, No. 1, Xikang Road, Nanjing, 210098, China. E-mail: chehuinan@hhu.edu.cn
[b]Key Laboratory of Advanced Display Material and Devices, School of Materials Science and Engineering, Nanjing University of Science and Technology, 210094 Nanjing, China. E-mail: zhangkan@njust.edu.cn
†Electronic supplementary information (ESI) available. See DOI: https://doi.org/10.1039/d3nr01299a

have been made in the separation of photoinduced electron–hole pairs, especially in nanostructure design and band structure specifications.[26]

In particular, elemental doping[27] and defect control[28] are the most widely used methods to improve the photocatalytic activity of PCN. For instance, PCN that has been doped with alkali metals (K^+ or Na^+) displays a wide spectrum of light absorption and high separation efficiency of charge. As another example, nonmetallic dopants such as O or S are used to improve the selectivity of PCN for H_2O_2 formation.[29–33] In addition, there are also many relevant literature reports stating that the separation efficiency of electron–hole pairs can be improved by introducing pollutants as hole traps, thus accelerating the ORR.[34–36] Given that both dopants and defects may change the electronic structure, adding flaws while doping foreign elements might improve light absorption and encourage charge separation. The narrowing of the band gap and the improvement of light absorption allow for the production of additional photoelectrons and holes. In addition, by facilitating charge separation, more available electrons can be captured and participate in surface reactions.[37–39] Thus, the degradation of OXC with simultaneous H_2O_2 generation is of particular interest for the development of wastewater treatment since H_2O_2 is an environmentally friendly oxidizing agent that under certain conditions can generate the highly reactive $^{\bullet}OH$.

Herein, multi-heteroatom-doped PCN (K, P, O-CN) was prepared by a simple thermal shrinkage method. The obtained K, P, O-CN_x not only greatly improved the charge separation efficiency but also significantly enhanced the O_2 activation. The results showed that K, P, O-CN_5 had the highest photocatalytic activity to produce H_2O_2, and the apparent rate constant of OXC removal was 8.47 times higher than that of the pure PCN. Quenching experiments and electron spin resonance (ESR) analysis confirmed that the multi-heteroatom doped PCN effectively promotes the activation of O_2, thus realizing the efficient generation of H_2O_2 and degradation of OXC.

2.   Experimental section

2.1.   Preparation of PCN and K, P, O-CN_x

Normally, 10 g of urea and a series of varying quantities of potassium dihydrogen phosphate (KH_2PO_4) are added to the crucible to be fully ground into a powder. Then, the ground powder is calcined in a Muffle furnace under 550 °C for 4 h at a heating rate of 5 °C min^{-1}. Then the resulting solid is ground again into a powder. The quantities of KH_2PO_4 were 0.1 g, 0.3 g, 0.5 g, and 1.5 g, respectively, and the photocatalysts were named K, P, O-CN_1, K, P, O-CN_3, K, P, O-CN_5, and K, P, O-CN_{15}. The preparation process of PCN was also the same as that for K, P, O-CN_x, except for not adding potassium dihydrogen phosphate.

2.2.   Characterization

The structure and morphology of the photocatalysts were analyzed by X-ray diffraction (XRD, Rigaku, SmartLab). Ultraviolet spectrophotometry (UV-3600, Shimadzu, Japan) with standard $BaSO_4$ powder as a reference was carried out to study the UV-vis diffuse reflectance spectra (DRS) of the prepared samples. What is more, the chemical structure of the photocatalysts was characterized using X-ray photoelectron spectroscopy (XPS; Thermo Scientific K-Alpha$^+$, USA) and Fourier transform infrared (FTIR, Tensor 27, Bruker Optics, German) spectroscopy. Photoluminescence spectroscopy (PL) was performed on a fluorescence spectrophotometer F-7000 (Hitachi, Japan) with a laser excitation source of 360 nm. Electron spin resonance (ESR, EOL JES-FA200 EER) spectroscopy with 5,5-dimethy1-1 pyrroline N-oxide (DMPO) and 2,2,6,6-tetramethyl-L-piperidine-N-oxyl (TEMPO) as spin label molecules was used to detect the active species in the sample. Temperature-programmed desorption (TPD, AutoChem1 II 2920) was used to measure the O_2 adsorption on the samples. Additionally, the Brunauer–Emmett–Teller (BET) method was applied using a Micromeritics ASAP 2460 3.01 in order to determine the precise surface areas of samples.

2.3.   Photoelectrochemical performance measurement

On an electrochemical workstation (CHI660D, Chenhua, China) with the standard three electrodes, the electrochemical impedance spectra (EIS), the photoelectrochemical properties comprising the photocurrent response (PCR), and the Mott–Schottky plot were measured. The electrochemical workstation consists of the standard Ag/AgCl, Pt plate and working electrode. The sample was prepared as follows: 40 mg of the prepared sample was mixed with 100 μL of Nafion, 500 μL of ethylene glycol, and 500 μL of ethanol in a 2 mL centrifuge tube, and then ultrasonic stirring was performed until the solution was uniform. Then 100 μL of the obtained solution was evenly spread on an indium tin oxide (ITO) glass conductive surface, which had an effective surface area of 1 cm^2. In addition, the photocurrent response (PCR) and electrochemical impedance spectra (EIS) of the samples were tested in 0.5 M Na_2SO_4 aqueous solution and 5 mM Fe $[(CN)_6]^{3-}/^{4-}$ solution, respectively.

In addition, on a Chenhua CHI 760E electrochemical workstation with the standard three electrodes, the rotating disk electrode (RDE) was run. The Ag/AgCl electrode and Pt plate were the same as above. The working electrode was prepared as follows: continuous ultrasonic treatment was used to equally distribute 5 mg of catalysts in 1 mL of an ethanol solution containing 100 μL of Nafion. A clean glassy carbon electrode received 5 mL of the produced sample in an even layer, and it was allowed to air dry there at room temperature. In an oxygen-saturated phosphate buffer solution with a pH of 7, the linear sweep voltammetry (LSV) was studied. The rotational speeds are 400 rpm, 800 rpm, 1200 rpm, 1600 rpm, and 2500 rpm, respectively. The LSV curves were produced at a scan rate of 5 mV s^{-1}.

2.4.   Photocatalytic activity of H_2O_2 generation

Photocatalytic activity evaluation was performed under visible light with a 300 W Xe lamp ($\lambda > 420$ nm) and the experimental

temperature was kept at 25 °C by condensed water device. The experimental steps for the photocatalytic production of H_2O_2 were as follows: 25 mg of catalyst and 50 mL of deionized water solution were put into a beaker. After 5 min of ultrasonic stirring, the solution was uniformly oxygenated in the dark and stirring continued for 30 min. Before starting the photocatalytic process, the lamp needed to be warmed for 30 minutes. During the photocatalytic reaction, 2 mL of suspension was collected every 10 min. The obtained suspension was centrifuged to remove the precipitate and take the supernatant. The supernatant was chromogenically reacted with horseradish peroxidase (HRP) and *N,N*-diethyl-*p*-phenylenediamine sulfate (DPD) to determine the H_2O_2 concentration with an absorption peak at 551 nm.

2.5. Photocatalytic degradation activities

The ability of the as-prepared samples to degrade OXC was determined in a quartz glass vessel, and the visible light source was a 300 W Xe lamp ($\lambda > 420$ nm). Condensed water device was used to maintain the experimental temperature at 293 K. The reaction solution was prepared as follows: 25 mg of photocatalyst was dispersed in 50 mL of OXC solution at 50 ppm. After 5 min of ultrasonic stirring, the mixture was evenly oxygenated in the dark while being stirred for another 30 min. Then, every 10 min during the 60-minute-long degradation process, 1.5 mL of the reaction solution was drawn into the centrifuge tube and centrifuged. The upper clarification fluid was measured using liquid chromatography (HPLC). The mobile phases were composed of acetonitrile and water with a volume ratio of 30 : 70. Furthermore, the flow rate, injection volume, and testing cycle were 1 mL min^{-1}, 10 μL and 7.1 min, respectively. In addition, according to the formula $\ln(C_0/C_t) = K_{app}t$, the photocatalytic degradation rate constant can be evaluated by the pseudo first-order kinetics. Ethylenediamine tetra-acetic acid disodium salt (EDTA-2Na) and argon (Ar) gas were used as scavengers for holes (h^+) and superoxide radicals ($^·O_2^-$), respectively, and the contributions of h^+ and $^·O_2^-$ were estimated by the following formula:

$$CR\, h^+ = \frac{K_{h^+}}{K_{app}} \approx \frac{(K_{app} - K_{EDTA-2Na})}{(K_{app})} \qquad (1)$$

$$CR\, ^·O_2^- \frac{K_{·O_2^-}}{K_{app}} \approx \frac{(K_{app} - K_{Ar})}{(K_{app})} \qquad (2)$$

where C_t and C_0 are the concentration of oxcarbazepine at time t and initial time. K_{app} denotes the apparent rate constant. Furthermore, in the presence of the respective radical scavengers, K_{Ar} and $K_{EDTA-2Na}$ are the apparent rate constants throughout the OXC degradation process.

2.6. DFT calculations

DFT calculations were performed using the Gaussian 16, Revision C.01 software package (Frisch, 2019).[40,41] Calculations of frequencies were carried out to make sure the stability configuration did not have any imaginary frequencies. The self-con-

sistent reaction field (SCRF) based on the implicit solvation model density (SMD) model was used to account for the solvent impact of H_2O.[42] The frontier molecular orbital, density of states (DOS), interaction region indicator (IRI),[43] hole–electron analysis[44] and interfragment charge transfer (IFCT) were calculated with Multiwfn 3.8(dev).[45] VMD 1.9.3 was used to display all images of structures and isosurfaces.[46] The def2-TZVPP basis set based on ORCA 4.2.1 was used in conjunction with PWPB95-D3(BJ) double-hybrid functionals to calculate the single-point energy.[47] The adsorption energy (E_{ads}) of O_2 was calculated as follows:

$$E_{ads}(O_2) = E(*O_2) - E(*) - E(O_2) \qquad (3)$$

where $E(*O_2)$, $E(*)$ and $E(O_2)$ are the total energy of samples with O_2 adsorbates on the surface, the energy of pristine samples surface and O_2, respectively.

3. Results and discussion

3.1. Structure and morphology analysis

To clarify the material structure of the as-synthesized catalysts, a series of characterization analyses were executed including XRD patterns, FT-IR spectra and XPS spectra. As shown in Fig. 1a,
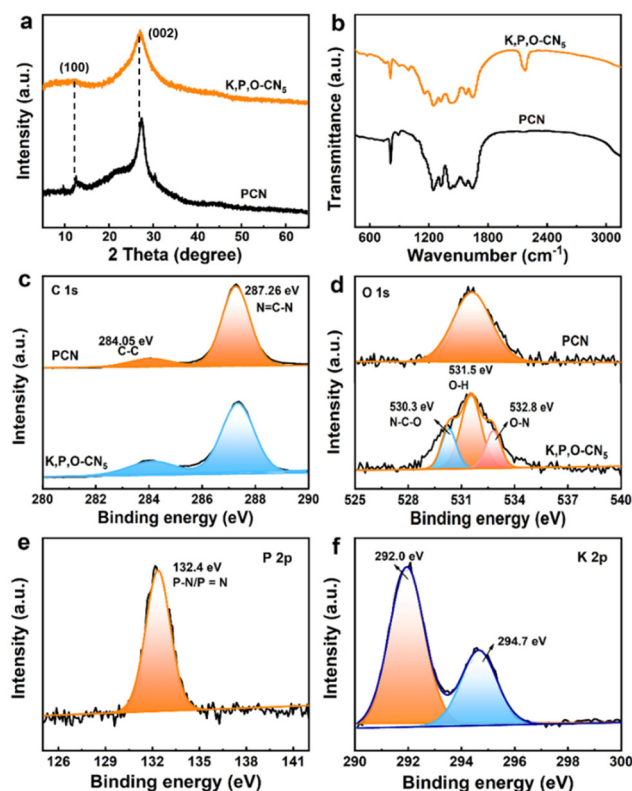

Fig. 1 (a) XRD patterns, (b) FT-IR spectra of PCN and K, P, O-CN$_5$. (c and d) The C 1s and N 1s high-resolution XPS spectra of PCN and K, P, O-CN$_5$. The (e) P 2p and (f) K 2p high-resolution XPS spectra of PCN and K, P, O-CN$_5$.

both PCN and K, P, O-CN$_5$ exhibit a similar crystalline structure, showing that multi-heteroatom doping does not change the structure of PCN.

It is worth noting that there are two obvious diffraction peaks at 12.9° (100) and 27.8° (002) in PCN which could be ascribed to the planar ordered arrangement of tri-*s*-triazine and interlayer superposition of conjugated aromatic hydrocarbons.[48–51] Specifically, compared with PCN, the (002) peak of K, P, O-CN$_5$ has shifted significantly, which indirectly proves that K, P and O elements are introduced into the PCN structure. In addition, the FT-IR spectra were obtained to further make out the interior structure of catalysts (Fig. 1b). In detail, the peaks of PCN and K, P, O-CN$_5$ located at 810 cm^{-1} and 1200–1600 cm^{-1}, respectively, could be put down to the triazine unit and aromatic C–N heterocyclic units. Notably, a new characteristic peak appears at 2200 cm^{-1}, which belongs to the cyano group (–C≡N). To get insight into the local electronic structure, the XPS spectra of the as-prepared samples were obtained. From the C 1s XPS spectra in Fig. 1c, the typical peaks at 284.50 eV and 287.26 eV are attributed to the C–C/C=C bonds and N=C–N bonds, respectively.[52,53] What is more, the XPS spectra in Fig. S1† for N 1s XPS spectra show characteristic CN=C, N-[C]$_3$ and C-NH$_x$ peaks at 397.8 eV, 399.4 eV and 400.4 eV, respectively. Analogously, for O 1s XPS spectra in Fig. 1d, compared to PCN, two new peaks at 530.3 eV and 532.8 eV are attributed to the N–C–O and O–N bonds, demonstrating the successful doping of the O element. What is more, the P 2p XPS spectra of PCN and K, P, O-CN$_5$ can be resolved into one main peak at 132.4 eV (Fig. 1e), which can be assigned to P–N/P=N. Further, the main K$_{1/2p}$ and K$_{3/2p}$ peaks of K 2p are located at 294.7 and 292.0 eV, respectively (Fig. 1f), which are consistent with the binding energy of the K–N bond. In brief, the above characterization studies all demonstrate the successful doping of K, P and O elements into PCN. Furthermore, the morphology of PCN and K, P, O-CN$_5$ was tested by TEM. The TEM images of PCN and K, P, O-CN$_5$ display the analogous nanosheet structure, suggesting that K, P and O co-doping did not change the morphology of PCN (Fig. S2a and b†). The elemental mapping images of K, P, O-CN$_5$ show a uniform distribution of C, N, O, P and K elements (Fig. S2c†), which further confirms the above experimental results.

3.2. Photocatalytic H$_2$O$_2$ production activity of as-prepared samples

The performance of PCN and K, P, O-CN$_x$ samples for photocatalytic production of H$_2$O$_2$ was investigated. Fig. 2a shows that the H$_2$O$_2$ yield of K, P, O-CN is improved to some degree compared with that of pure PCN. Obviously, with the increase in the concentration of K$_2$HPO$_4$, the H$_2$O$_2$ yield is also increased. Compared to PCN, the H$_2$O$_2$ yield of K, P, O-CN$_5$ is the highest, which reaches 46.46 μM in 1 hour under pure water. However, the H$_2$O$_2$ yield of K, P, O-CN$_{15}$ decreases (Fig. S3–S7†), possibly because the concentration of K$_2$HPO$_4$ is too high, which destroys the structure of PCN. As shown in
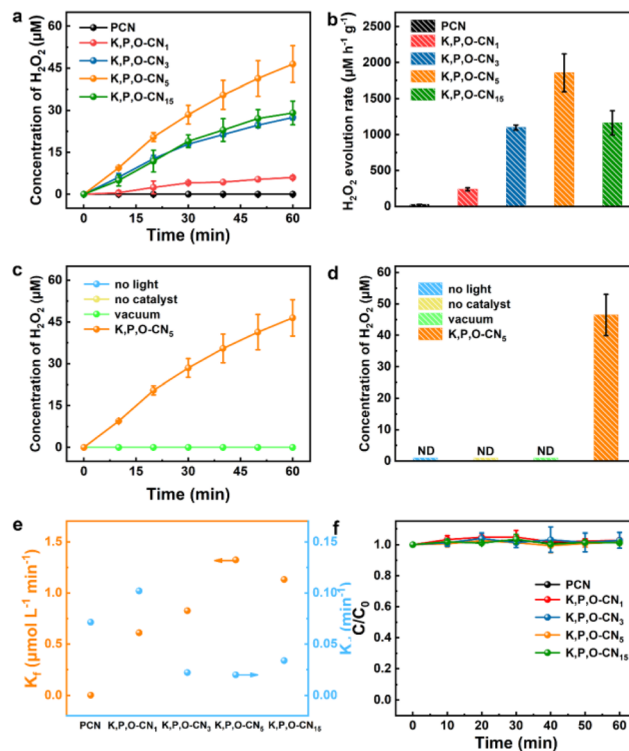

Fig. 2 (a) Photocatalytic H$_2$O$_2$ production, (b) H$_2$O$_2$ production rate of as-prepared samples. (c and d) Photocatalytic H$_2$O$_2$ production activity of K, P, O-CN$_5$ under different conditions. (e) Formation rate constant (K_f) and decomposition rate constant (K_d) for H$_2$O$_2$ production. (f) The photocatalytic decomposition of H$_2$O$_2$ (1 mM) under visible light irradiation.

Fig. 2b, it is found that the H$_2$O$_2$ generation of K, P, O-CN$_5$ with an ultrahigh rate of 1858 μM h^{-1} g^{-1} is about 1574.91 times that for pure PCN. The improvement of H$_2$O$_2$ production performance of K, P, O-CN$_5$ may be attributed to multi-heteroatom-doped PCN promoting O$_2$ activation. In addition, the conditions of H$_2$O$_2$ production are studied (Fig. 2c and d). It is found that there is no H$_2$O$_2$ detected in the absence of light or catalyst or in a vacuum, indicating that H$_2$O$_2$ is produced by the photocatalytic ORR.

Usually, the final concentration of H$_2$O$_2$ is determined by the amount of H$_2$O$_2$ produced and H$_2$O$_2$ decomposition. By assuming the corresponding zero-order kinetics for H$_2$O$_2$ formation and first-order kinetics for H$_2$O$_2$ decomposition, the concentration of H$_2$O$_2$ accumulated can be well described by the kinetic model, using the equation:

$$[\text{H}_2\text{O}_2] = \frac{K_f}{K_d}(1 - \exp(-K_d t)) \tag{4}$$

K_f and K_d are the rate constants of H$_2$O$_2$ formation (μM min^{-1}) and decomposition (min^{-1}), respectively. The values of K_f and K_d are estimated using the fitting data in Fig. 2a and eqn (1). As shown in Fig. 2e, the K_f value of K, P, O-CN$_5$ reaches a maximum (1.32 μM min^{-1}) that is 806 times that of PCN (0.00164 μM min^{-1}). Furthermore, K, P, O-CN$_5$ has the

lowest K_d (0.0198 min^{-1}), showing that H_2O_2 generated over K, P, O-CN$_5$ has excellent stability. Therefore, under a certain amount of H_2O_2 (initial concentration of H_2O_2 [C_0] = 1 mM), the decomposition performance of H_2O_2 under visible-light radiation was further conducted. Apparently, H_2O_2 almost never breaks down in 1 h, which leads to excellent photocatalytic H_2O_2 production.

3.3. Photocatalytic degradation activity of as-prepared samples

To demonstrate that OXC can be used as a sacrificial reagent to promote O$_2$ activation to produce H_2O_2, photocatalytic degradation of OXC was performed. As shown in Fig. 3a, the yield of K, P, O-CN$_5$ photocatalytic production of H_2O_2 in a pure aqueous solution was substantially higher compared to PCN, reaching 46.5 µM. What is more, the yield of H_2O_2 (109.7 µM) for K, P, O-CN$_5$ was obviously enhanced in the OXC solution at a concentration of 50 ppm. Most importantly, as displayed in Fig. 3b, PCN degraded 43.6% of OXC within 60 min, while K, P, O-CN$_5$ degraded 97.0%. Correspondingly, the apparent rate constant of K, P, O-CN$_5$ for OXC removal is 8.47 times higher than that of the pure PCN (Fig. S8†). In addition, the photocatalytic production of H_2O_2 and degradation activity at different concentrations of

OXC are shown in Fig. S9 and S10.† Evidently, multi-heteroatom-doped PCN promotes O$_2$ activation for the *in situ* generation of H_2O_2 and the degradation of OXC. In order to verify the contribution of different free radicals to the degradation of OXC by K, P, O-CN$_5$, quenching experiments were performed. During the degradation process, ethylenediamine tetraacetic acid disodium salt (EDTA-2Na) and argon (Ar) are responsible for scavenging holes (h$^+$) and superoxide radicals ($^\bullet$O$_2^-$), respectively. The degradation efficiency of K, P, O-CN$_5$ was found to decrease significantly after the addition of EDTA. The contribution rate of h$^+$ in the photocatalytic degradation reaction was calculated to be 87.5% (Fig. 3c and d), indicating that h$^+$ plays a dominant role in the degradation. The above experimental results also prove that OXC as a hole trapping agent not only accelerates the separation of carriers but also promotes the activation of O$_2$ to produce H_2O_2. However, it is noteworthy that when isopropanol (IPA) is added to the solution, the photocatalytic degradation performance of OXC is significantly improved. The ability to improve the above performance is attributed to the *in situ* formation of more $^\bullet$OH. Obviously, the electron spin resonance (ESR) spectra directly show the existence of more h$^+$ and $^\bullet$OH in K, P, O-CN$_5$ than in the PCN system (Fig. 3e and f), matching well the higher photocatalytic activity of K, P, O-CN$_5$ as compared to PCN.

3.4. Mechanism analysis of photocatalytic performance improvement

To further investigate the mechanism of photocatalytic H_2O_2 production, the nitrogen adsorption–desorption isotherms of PCN and K, P, O-CN$_5$ were tested. Compared to PCN, K, P, O-CN$_5$ has a larger specific surface area (Fig. 4a), which indicates that there are more active sites on the surface of K, P, O-CN$_5$ for photocatalytic H_2O_2 production.[54,55] As shown in Fig. 4b, K, P, O-CN$_5$ has stronger O$_2$-TPD signals, unraveling that the oxygen adsorption capacity of K, P, O-CN$_5$ is stronger than that of PCN, thus favoring the occurrence of the ORR. In addition, according to the electron spin-resonance (ESR), the DMPO-$^\bullet$O$_2^-$ signal of K, P, O-CN$_5$ is stronger than that of PCN (Fig. 4c), illustrating that H_2O_2 is likely to be produced by a sequential two-step ORR. As we all know, O$_2$ can accept one electron to form $^\bullet$O$_2^-$, and then the $^\bullet$O$_2^-$ takes another electron to generate H_2O_2 through a sequential two-step one electron ORR.[56] To further gain insight into the electron transfer in H_2O_2 production, the rotating disk electrode (RDE) was used. Fig. 4d and e shows linear sweep voltammetry (LSV) curves at different rotational speeds. It is found that the strength of LSV increases with the increase of the rotational speed, and the average numbers of transferred electrons (n) fitted by the Koutecky–Levich plots are calculated to be 2.28 and 0.91 for K, P, O-CN$_5$ and PCN, respectively (Fig. 4f). Therefore, compared with PCN, it is easier for K, P, O-CN$_5$ to produce H_2O_2 through the 2e$^-$ ORR.

The UV-vis DRS and the corresponding band structure of PCN and K, P, O-CN$_5$ were explored to further clarify the intrin-
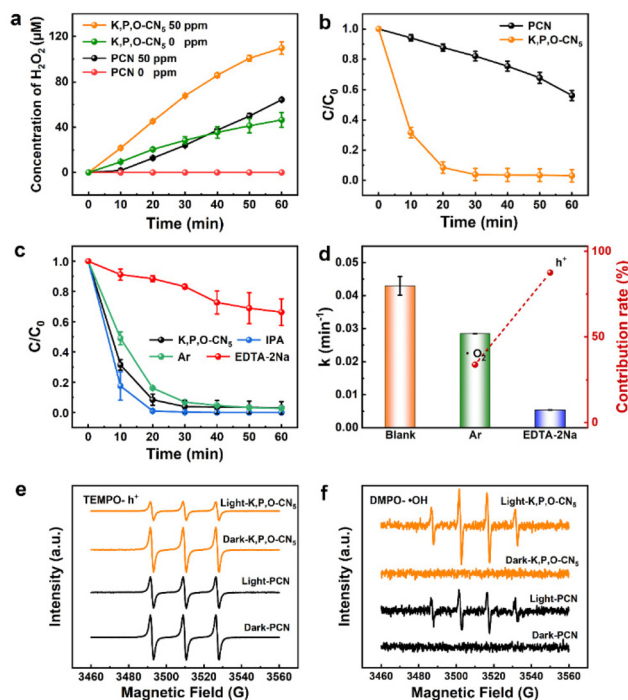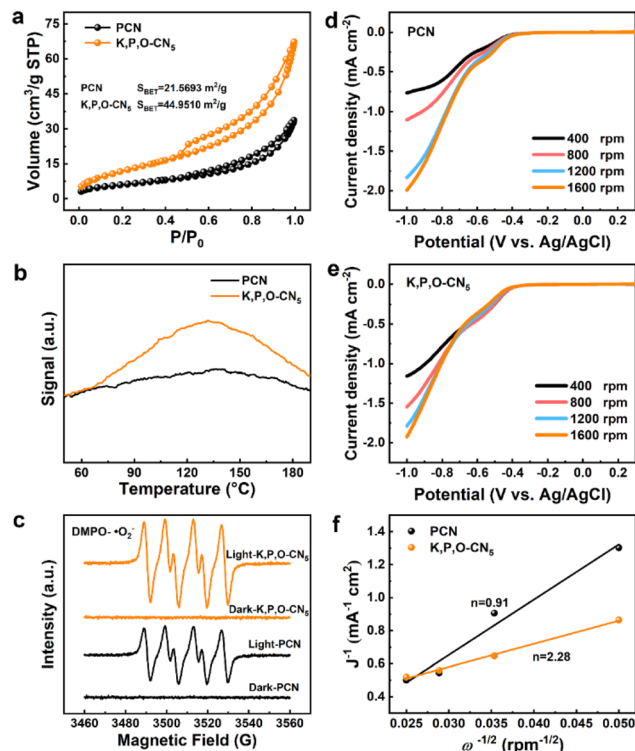

Fig. 3 (a) Photocatalytic H_2O_2 production of PCN and K, P, O-CN$_5$ with OXC solution at different concentrations under visible light irradiation. (b) The photocatalytic decomposition curves of OXC with PCN and K, P, O-CN$_5$ under visible light irradiation. (c) The decomposition curves of OXC on K, P, O-CN$_5$ with different radical scavengers. (d) The first-order reaction kinetic constants and free radical contribution of OXC degradation on K, P, O-CN$_5$. ESR spectra of the (e) TEMPO-h$^+$ and (f) DMPO-$^\bullet$OH.

Fig. 4 (a) N_2 adsorption/desorption isotherms and (b) O_2-TPD spectra of K, P, O-CN_5 and PCN. (c) ESR spectra of DMPO-$\cdot O_2^-$ adduct of K, P, O-CN_5 and PCN. (d) PCN and (e) K, P, O-CN_5 measured on RDE at different rotating speeds. (f) Koutecky–Levich plots of data obtained by RDE analysis of PCN and K, P, O-CN_5.

Fig. 5 (a) UV-vis DRS (inset: Tauc plots of as-prepared catalysts) and (b) corresponding band structures of PCN and K, P, O-CN_5. (c) PL, (d) PCR, (e) EIS and (f) LSV curves of PCN and K, P, O-CN_5.

sic structural merits for photocatalytic activity.[57] Apparently, Fig. 5a shows that K, P, O-CN_5 has a broader range of light absorption compared to PCN and the fitted band gap energies (E_g) of PCN and K, P, O-CN_5 are 2.95 eV and 2.76 eV. What is more, the flat band potentials (E_{FB}) of PCN and K, P, O-CN_5 are −1.35 V and −0.91 V, respectively, measured by Mott–Schottky analysis (Fig. S11 and S12†), which are converted to −1.15 V and −0.71 V (vs. NHE) in accordance with the relationship between E_{FB} and conduction band CB over an n-type semiconductor. Integrated with the equation $E_g = E_{VB} - E_{CB}$, the calculated valence band (VB) positions of PCN and K, P, O-CN_5 are 1.8 V and 2.05 V, respectively. Therefore, the corresponding band structures of PCN and K, P, O-CN_5 were obtained, as shown in Fig. 5b. It can be seen that both PCN and K, P, O-CN_5 satisfy the needs of O_2 reduction E (O_2/H_2O_2 = 0.68 V vs. NHE) and H_2O oxidation E (H_2O/H_2O_2 = 0.68 V vs. NHE).[58] Specifically, the narrower band gap and more positive VB means more efficient carrier separation and greater oxidizability. In addition to the light absorption capacity and band structure, the electrochemical properties of as-prepared samples also have a great influence on the catalytic performance. As shown in Fig. 5c, the K, P, O-CN_5 possesses a lower photoluminescence (PL) peak, which is due to the K, P, O element doping changing the efficiency of carrier separation within the catalysts. Analogously, the
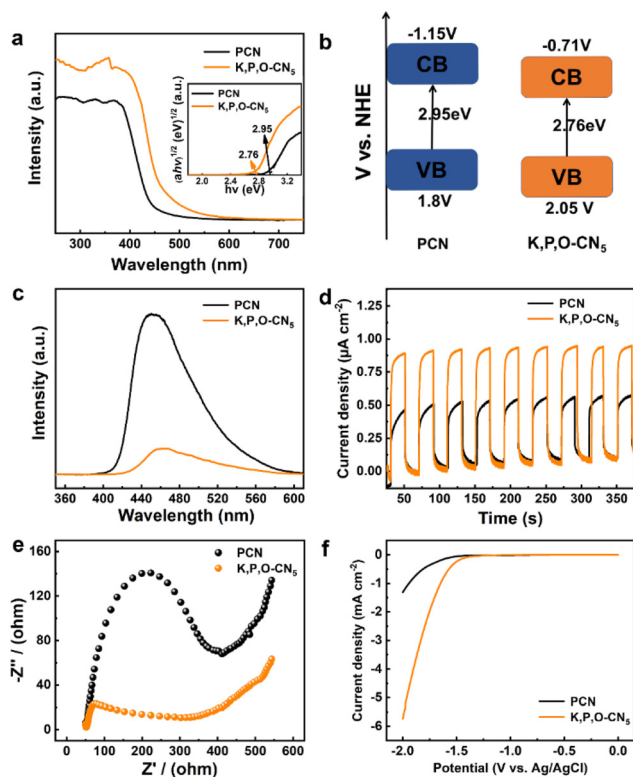
higher photocurrent response (PCR) density and smaller EIS of K, P, O-CN_5 than PCN mean that K, P, O-CN_5 is endowed with a stronger and more available charge separation efficiency (Fig. 5d and e).[59,60] Moreover, excellent photoelectric performance was also mapped by the LSV response and EPR (Fig. 5f and Fig. S13†).

3.5. Possible degradation pathways

The main intermediates produced during the degradation of OXC were revealed by high-performance liquid chromatography–mass spectrometry (HPLC-MS) analysis, as shown in Fig. 6a, Fig. S14 and Table S1.† OXC was attacked by $\cdot$OH to produce P1 (m/z = 268), after which there were two degradation pathways. The first pathway was attack by –$CONH_2$ to produce P2 (m/z = 225), then P2 was degraded to P3 (m/z = 207), and P3 was converted to P4 (m/z = 179). The second pathway is that P1 continues to be attacked by $\cdot$OH, which eventually transforms into P8 (m/z = 282). In addition, there is another pathway in the system. OXC may also react with $\cdot$OH and –$CONH_2$ to form P9 (m/z = 223), and P9 undergoes benzilic acid rearrangement to form P10 (m/z = 223). P10 rearranges and reacts with –CO to form P12 (m/z = 195). After the rearrangement of P12, it reacts with $\cdot$OH to eventually convert to P14 (m/z = 211). In addition, the interfacial interaction between OXC and catalyst was first investigated by theoretical calculations based on DFT. As shown in Fig. 6b–d,
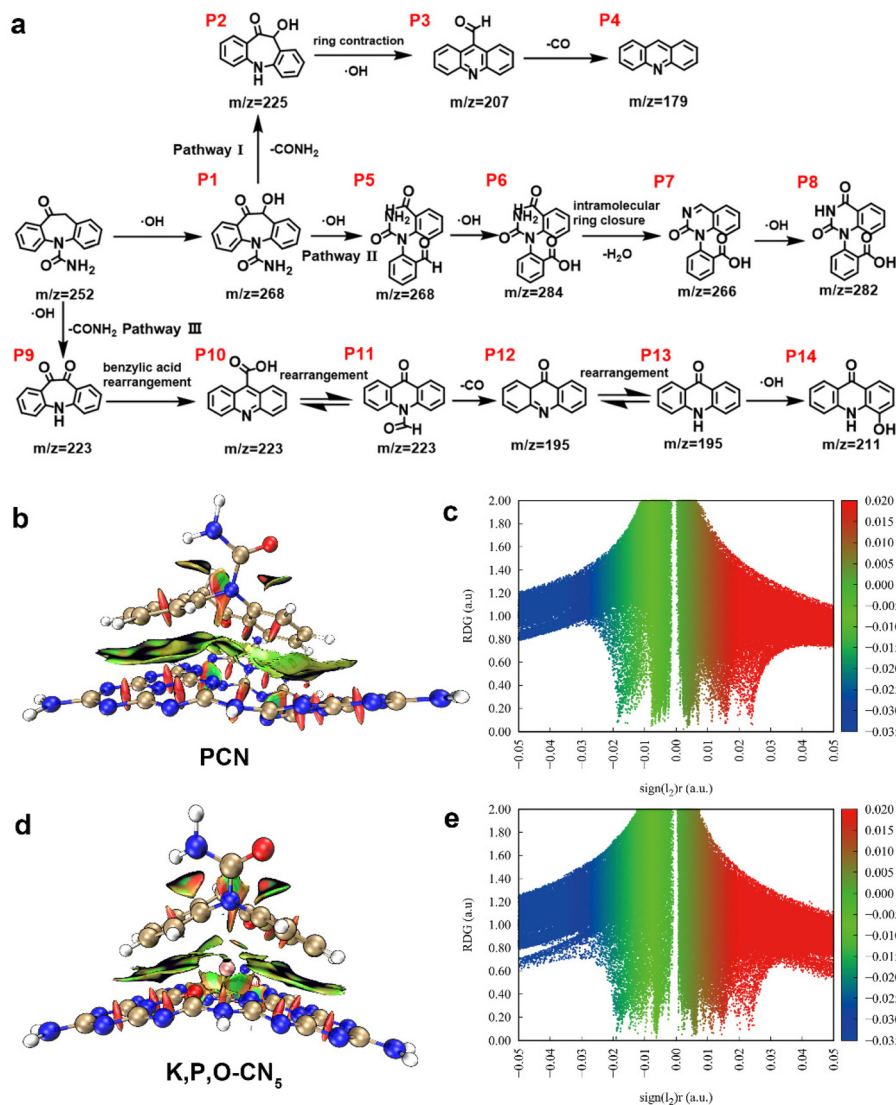
Fig. 6 (a) Presumed OXC degradation pathways in K, P, O-CN$_5$. (b) Isosurface map of IRI and (c) the plots of RDG *versus* electron density (ρ) multiplied by the sign of the second Hessian eigenvalue ($\lambda2$) of PCN. (d) Isosurface map of IRI and (e) the plots of RDG *versus* electron density (ρ) multiplied by the sign of the second Hessian eigenvalue ($\lambda2$) of K, P, O-CN$_5$.

the interaction region index (IRI) demonstrates the weak contact (π–π) between OXC and PCN as well as K, P, O-CN$_5$, respectively.[61] In addition, the weak interactions between OXC and PCN as well as K, P, O-CN$_5$, respectively, were examined by lowering the density gradient (RDG). As shown in Fig. 6c–e, blue, green and red represent strong gravitational, van der Waals and repulsive forces, respectively. The results of RDG show that there are van der Waals forces between OXC and K, P, O-CN$_5$, which are greater than those between OXC and PCN.

3.6. DFT calculations

In order to further analyze the catalytic mechanism, PCN and K, P, O-CN$_5$ conjugated polymer system models were established based on DFT. As shown in Fig. 7e, the adsorption energy of O$_2$ adsorption at different sites of PCN is roughly the same. In contrast, the adsorption energy of O$_2$ adsorption for K, P, O-CN$_5$ is improved to a certain extent, and the adsorption energy near the phosphorus atom is the largest (-0.179 eV), as shown in Fig. 7d. DFT was also used to investigate the density of states (DOS), aiming to show how the band structure had changed. As shown in Fig. 7a and b, the K, P, O-CN$_5$ conjugated polymer has small bandgaps in comparison with PCN. Notably, as seen in Fig. 7c, the nitrogen ρ_z orbitals and C–N orbitals are primarily responsible for PCN's highest occupied molecular orbit (HOMO) and lowest occupied molecular orbit (LUMO).[62] The HOMO and LUMO of K, P, O-CN$_5$ conjugated polymers, on the other hand, are scattered on various structural units, showing a spatial separation of HOMO and LUMO. The above results prove that K, P, O-CN$_5$ has higher O$_2$ adsorption efficiency and better photocatalytic performance.
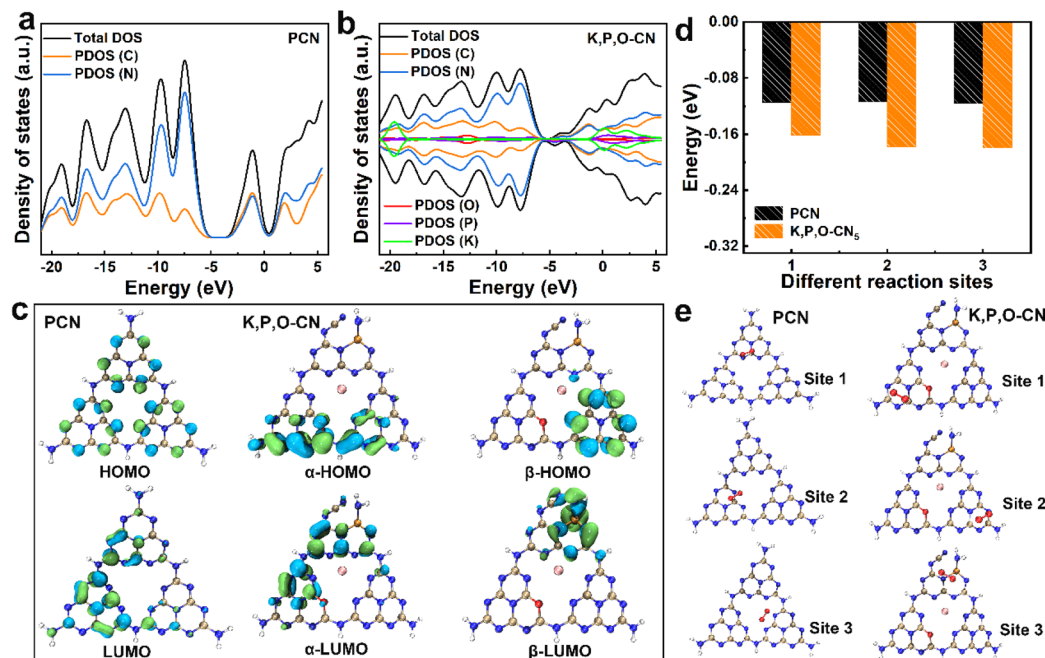
Fig. 7 (a and b) DOS of PCN and K, P, O-CN$_5$. (c) Electronic structure of the optimized HOMO and LUMO of pure PCN and K, P, O-CN$_5$. (d) The adsorption energy of O$_2$ for PCN and K, P, O-CN$_5$ at different sites. (e) The structures after O$_2$ adsorption at different sites of PCN and K, P, O-CN$_5$. Green and blue isosurfaces represent electron and hole distributions, respectively. The isosurface value is 0.002 e Å^{-3}. Gray, blue, red, white, pink and golden represent C, N, O, H, K and P, respectively.

4. Conclusions

In conclusion, multi-heteroatom-doped PCN was prepared by a simple thermal shrinkage method. The K, P, O-CN$_5$ exhibits the highest photocatalytic activity for H$_2$O$_2$ production (1858 μM h^{-1} g^{-1}), which is about 1574.91 times that for pure PCN. In addition, the apparent rate constant of OXC degradation in K, P, O-CN$_5$ reaches 0.0491 min^{-1}, which is 8.47 times that of photocatalysis over pure PCN. The doping of multiple heteroatoms in PCN not only speeds up the efficiency of carrier separation but also increases the adsorption/activation capacity of O$_2$, thus improving the 2e$^-$ ORR of H$_2$O$_2$ synthesis. DFT calculation further proved that K, P, O-CN$_5$ showed better O$_2$ adsorption capacity. This work provides a new vision for PCN modification and water environmental treatment.

Conflicts of interest

There are no conflicts to declare.

Acknowledgements

References

1 T. C. Liu, K. Yin, C. B. Liu, J. M. Luo, J. Crittenden, W. Q. Zhang, S. L. Luo, Q. Y. He, Y. X. Deng, H. Liu and D. Y. Zhang, *Water Res.*, 2018, **147**, 204–213.

2 L. J. Bu, S. Q. Zhou, Z. Shi, C. Bi, S. M. Zhu and N. Y. Cao, *Sep. Purif. Technol.*, 2017, **178**, 66–74.

3 H. Fenet, L. Arpin-Pont, A. Vanhoutte-Brunier, D. Munaron, A. Fiandrino, M. M. Bueno, C. Boillot, C. Casellas, O. Mathieu and E. Gomez, *Environ. Int.*, 2014, **68**, 177–184.

4 Z. Li, H. Fenet, E. Gomez and S. Chiron, *Water Res.*, 2011, **45**, 1587–1596.

5 W. Liu, P. F. Wang, Y. H. Ao, J. Chen, X. Gao, B. H. Jia and T. Y. Ma, *Adv. Mater.*, 2022, **34**, 2202508.

6 M. C. V. M. Starling, R. P. de M. Neto, G. F. F. Pires, P. B. Vilela and C. C. Amorim, *Sci. Total Environ.*, 2021, **786**, 147448.

7 E. Cako, R. D. C. Soltani, X. Sun and G. Boczkaj, *Chem. Eng. J.*, 2022, **439**, 135354.

8 L. Ge, K. Moor, B. Zhang, Y. L. He and J. H. Kim, *Nanoscale*, 2014, **6**, 13579–13585.

9 Y. H. Sun, X. X. Chen, L. Liu, F. Xu and X. C. Zhang, *Sci. Total Environ.*, 2021, **770**, 145203.

10 C. H. Fang, H. L. Jia, S. Chang, Q. F. Ruan, P. Wang, T. Chen and J. F. Wang, *Energy Environ. Sci.*, 2014, **7**, 3431–3438.

11 U. Ushani, X. Q. Lu, J. H. Wang, Z. Y. Zhang, J. J. Dai, Y. J. Tan, S. S. Wang, W. J. Li, C. X. Niu, T. Cai, N. Wang and G. Y. Zhen, *Chem. Eng. J.*, 2020, **402**, 126232.

12 N. López, S. Plaza, A. Afkhami, P. Marco, J. Giménez and S. Esplugas, *Chem. Eng. J.*, 2017, **318**, 112–120.

13 J. Lee, U. V. Gunten and J. H. Kim, *Environ. Sci. Technol.*, 2020, **54**, 3064–3081.

14 Q. Li and F. T. Li, *Chem. Eng. J.*, 2021, **421**, 129915.

15 H. N. Che, X. Gao, J. Chen, J. Hou, Y. H. Ao and P. F. Wang, *Angew. Chem., Int. Ed.*, 2021, **60**, 25546–25550.

16 B. Zhu, B. Cheng, J. Fan, W. Ho and J. Yu, *Small Struct.*, 2021, **2**, 2100086.

17 W. Liu, P. F. Wang, J. Chen, X. Gao, H. N. Che, B. Liu and Y. H. Ao, *Adv. Funct. Mater.*, 2022, **32**, 2205119.

18 L. P. Xu, L. J. Li, L. Yu and J. C. Yu, *Chem. Eng. J.*, 2022, **431**, 134241.

19 Y. H. Zhao, D. X. Wang, H. N. Che, B. Liu and Y. H. Ao, *Environ. Funct. Mater.*, 2022, **1**, 316–324.

20 W. Ong, L. Tan, Y. Ng, S. Yong and S. Chai, *Chem. Rev.*, 2016, **116**, 7159–7329.

21 J. J. Liu, C. B. Xiong, S. J. Jiang, X. Wu and S. Q. Song, *Appl. Catal., B*, 2019, **249**, 282–291.

22 Q. H. Zhu and J. L. Zhang, *Environ. Funct. Mater.*, 2022, **1**, 121–125.

23 S. D. Sohn, Y. H. Kim, S. C. Jung, J. S. Kang, H. J. Han, K. S. Kim, K. Park and H. J. Shin, *ACS Catal.*, 2022, **12**, 5990–5996.

24 Y. Deng and J. D. Englehardt, *Water Res.*, 2006, **40**, 3683–3694.

25 B. J. Dramou, V. Shahb and J. M. Pinto, *Energy Environ. Sci.*, 2008, **1**, 395–402.

26 Y. Wu, H. N. Che, B. Liu and Y.H. Ao, *Small Struct.*, 2023, 2200371.

27 J. G. Song, H. T. Zhao, R. R. Sun, X. Y. Li and D. J. Sun, *Energy Environ. Sci.*, 2017, **10**, 225–235.

28 S. Gao, X. Wang, C. Song, S. Zhou, F. Yang and Y. Kong, *Appl. Catal., B*, 2021, **295**, 120272.

29 J. W. Fu, J. G. Yu, C. J. Jiang and B. Cheng, *Adv. Energy Mater.*, 2018, **8**, 1701503.

30 G. F. Liao, Y. Gong, L. Zhang, H. Y. Gao, G. J. Yang and B. Z. Fang, *Energy Environ. Sci.*, 2019, **12**, 2080–2147.

31 S. Y. Zhang, Y. Yang, Y. P. Zhai, J. Q. Wen, M. Zhang, J. K. Yu and S. Y. Lu, *Chin. Chem. Lett.*, 2023, **34**, 107652.

32 J. R. Ran, T. Y. Ma, G. P. Gao, X. W. Du and S. Z. Qiao, *Energy Environ. Sci.*, 2015, **8**, 3708–3717.

33 R. F. Du, K. Xiao, B. Y. Li, X. Han, C. Q. Zhang, X. Wang, Y. Zuo, P. Guardia, J. S. Li, J. B. Chen, J. Arbiol and A. Cabot, *Chem. Eng. J.*, 2022, **441**, 135999.

34 M. Xie, J. C. Tang, L. S. Kong, W. H. Lu, V. Natarajan, F. Zhu and J. H. Zhan, *Chem. Eng. J.*, 2019, **360**, 1213–1222.

35 F. Li, M. Tang, T. Li, L. L. Zhang and C. Hu, *Appl. Catal., B*, 2020, **268**, 118397.

36 S. Y. Chen, J. P. Yu, Z. F. Chai, W. Q. Shi and L. Y. Yuan, *Chem. Eng. J.*, 2023, **460**, 141742.

37 J. N. Li, J. Chen, Y. H. Ao, X. Gao, H. N. Che and P. F. Wang, *Sep. Purif. Technol.*, 2022, **281**, 119863.

38 X. Y. Wang, L. B. Sang, L. Zhang, G. Yang, Y. H. Guo and Y. X. Yang, *J. Alloys Compd.*, 2023, **941**, 168921.

39 C. Yang, Y. T. Hou, G. Q. Luo, J. G. Yua and S. W. Cao, *Nanoscale*, 2022, **14**, 11972–11978.

40 C. Adamo and V. Barone, *J. Chem. Phys.*, 1999, **110**, 6158–6170.

41 S. Grimme, S. Ehrlich and L. Goerigk, *J. Comput. Chem.*, 2011, **32**, 1456–1465.

42 F. Weigend and R. Ahlrichs, *Phys. Chem. Chem. Phys.*, 2005, **7**, 3297–3305.

43 Z. Liu, T. Lu and Q. Chen, *Carbon*, 2020, **165**, 461–467.

44 T. Lu and F. Chen, *J. Comput. Chem.*, 2012, **33**, 580–592.

45 W. Humphrey, A. Dalke and K. Schulten, *J. Mol. Graphics*, 1996, **14**, 33–38.

46 L. Goerigk and S. Grimme, *J. Chem. Theor. Comput.*, 2010, **7**, 291–309.

47 F. Neese, *Science*, 2018, **8**, 1327.

48 Z. F. Chen, S. C. Lu, Q. L. Wu, F. He, N. Q. Zhao, C. N. He and C. S. Shi, *Nanoscale*, 2018, **10**, 3008–3013.

49 Y. Wu, J. Chen, H. N. Che, X. Gao, Y. H. Ao and P. F. Wang, *Appl. Catal., B*, 2022, **307**, 121185.

50 L. H. Lin, C. Wang, W. Ren, H. H. Ou, Y. F. Zhang and X. C. Wang, *Chem. Sci.*, 2017, **8**, 5506–5511.

51 Y. Y. Wen, J. Chen, X. Gao, W. Liu, H. N. Che, B. Liu and Y. H. Ao, *Nano Energy*, 2023, **107**, 108173.

52 H. N. Che, P. F. Wang, J. Chen, X. Gao, B. Liu and Y. H. Ao, *Appl. Catal., B*, 2022, **316**, 121611.

53 Y. J. Zhou, L. X. Zhang, W. M. Huang, Q. L. Kong, X. Q. Fan, M. Wang and J. L. Shi, *Carbon*, 2016, **99**, 111–117.

54 Y. Xia, B. Cheng, J. J. Fan, J. G. Yu and G. Liu, *Small*, 2019, **15**, 201902459.

55 W. Yan, Y. Yu, H. H. Zou, X. F. Wang, P. Li, W. Y. Gao, J. Z. Wang, S. M. Wu and K. J. Ding, *Sol. RRL*, 2018, **2**, 1800058.

56 G. D. Liu, H. Q. Deng, J. Greeley and Z. H. Zeng, *Chin. J. Catal.*, 2022, **43**, 3126–3133.

57 Q. Zhang, J. Chen, X. Gao, H. N. Che, P. F. Wang and Y. H. Ao, *Appl. Catal., B*, 2018, **239**, 578–585.

58 Q. Zhang, J. Chen, X. Gao, H. N. Che, Y. H. Ao and P. F. Wang, *J. Hazard. Mater.*, 2022, **430**, 128386.

59 K. Zhang, L. Y. Wang, X. W. Sheng, M. Ma, M. S. Jung, W. J. Kim, H. Y. Lee and J. H. Park, *Adv. Energy Mater.*, 2016, **6**, 1502352.

60 S. P. Wan, C. R. Dong, J. Jin, J. Li, Q. Zhong, K. Zhang and J. H. Park, *ACS Energy Lett.*, 2022, **7**, 3024.

61 Q. Zhang, J. Chen, X. Gao, H. N. Che, P. F. Wang, B. Liu and Y. H. Ao, *Sep. Purif. Technol.*, 2022, **300**, 121947.

62 H. N. Che, J. Wang, X. Gao, J. Chen, P. F. Wang, B. Liu and Y. H. Ao, *J. Colloid Interface Sci.*, 2022, **627**, 739–748.